

See discussions, stats, and author profiles for this publication at: <https://www.researchgate.net/publication/268392241>

Damage in spherical cellular membrane generated by the shock waves: Coarse-grained molecular dynamics simulation of lipid vesicle

ARTICLE *in* THE JOURNAL OF CHEMICAL PHYSICS · NOVEMBER 2014

Impact Factor: 2.95 · DOI: 10.1063/1.4901130 · Source: PubMed

CITATION

1

READS

70

2 AUTHORS, INCLUDING:



Yelena R. Slizberg

Army Research Laboratory

42 PUBLICATIONS 108 CITATIONS

SEE PROFILE

Damage in spherical cellular membrane generated by the shock waves: Coarse-grained molecular dynamics simulation of lipid vesicle

Yelena Sliozberg and Tanya Chantawansri

Citation: *The Journal of Chemical Physics* **141**, 184904 (2014); doi: 10.1063/1.4901130

View online: <http://dx.doi.org/10.1063/1.4901130>

View Table of Contents: <http://scitation.aip.org/content/aip/journal/jcp/141/18?ver=pdfcov>

Published by the [AIP Publishing](#)

Articles you may be interested in

[Coarse-grain simulations of active molecular machines in lipid bilayers](#)

J. Chem. Phys. **138**, 195101 (2013); 10.1063/1.4803507

[Coarse-grain model for lipid bilayer self-assembly and dynamics: Multiparticle collision description of the solvent](#)

J. Chem. Phys. **137**, 055101 (2012); 10.1063/1.4736414

[Coarse-grained simulations of membranes under tension](#)

J. Chem. Phys. **132**, 115101 (2010); 10.1063/1.3352583

[Pressure-temperature phase diagram for shapes of vesicles: A coarse-grained molecular dynamics study](#)

Appl. Phys. Lett. **95**, 143104 (2009); 10.1063/1.3245307

[Pores in bilayer membranes of amphiphilic molecules: Coarse-grained molecular dynamics simulations compared with simple mesoscopic models](#)

J. Chem. Phys. **121**, 1890 (2004); 10.1063/1.1752884



Damage in spherical cellular membrane generated by the shock waves: Coarse-grained molecular dynamics simulation of lipid vesicle

Yelena Sliozberg¹ and Tanya Chantawansri²

¹TKC Global at U.S. Army Research Laboratory, 4600 Deer Creek Loop, Aberdeen Proving Ground, Maryland 21005-5069, USA

²U.S. Army Research Laboratory, 4600 Deer Creek Loop, Aberdeen Proving Ground, Maryland 21005-5069, USA

(Received 11 August 2014; accepted 26 October 2014; published online 12 November 2014)

Traumatic Brain Injury is a major health issue that is hard to diagnose since it often occurs without signs of external injuries. While it is well known that exposure of biological cells to shock waves causes damage to the cell membrane, it is currently unknown by which mechanisms damage is caused, and how it depends on physical parameters such as shock wave velocity, shock pulse duration, or shock pulse shape. In this computational study, we use a coarse-grained model of the lipid vesicle as a generic model of a cell membrane to elucidate the general principles of the cellular damage induced by the shock wave direct passage through the cranium. Results indicate that the extent of the liposome compression does not strongly depend on the pressure pulse and that liposome extension is very sensitive to the change in the negative pressure phase. The structural integrity of the vesicle is altered as pores form in the lipid membrane at overall pressure impulses generated by supersonic shock waves, which are greater than $5 \text{ Pa} \cdot \text{s}$ at single or repetitive exposure. Consequently, these permeability changes may lead to changes in the influx of sodium, potassium, and calcium ions. © 2014 AIP Publishing LLC. [<http://dx.doi.org/10.1063/1.4901130>]

I. INTRODUCTION

Traumatic Brain Injury (TBI) is a major health issue that leads to a range of neurological and psychological impairments. It affects the general population where the Centers for Disease Control and Prevention reported in 2007 that each year 1.1×10^6 emergency room visits, 235 000 hospitalizations, and 50 000 deaths are a result of TBI.¹ In recent operations, hundreds of thousands of U.S. military personnel also sustained a mild form of TBI, often after exposure to an explosive blast. Mild TBI is hard to diagnose because it often happens without external injuries, and consequently mild TBI may not be identified until the service member returns home.²

The shock wave associated with primary TBI is a transient supersonic pressure wave with a rapid, less than 1-ms increase in pressure (compression), density, and temperature, which corresponds to the peak overpressure, followed by a rapid fall to nonlinear, microsecond phase of low pressure or tension. The most important part of the wave energy, in relation to TBI, are those transmitted into the body in the form of positive (compression), negative (tension), and shear stress waves.³ In the majority of TBI cases, the peak pressure is low. Even exposure to blasts of 10-atm peak pressure in a skull for a few milliseconds can result in death in unprotected subjects,⁴ where mild and moderate brain injuries occurred using the lateral fluid percussion model at pressures ranging from 100 to 300 kPa (1–3 atm).⁵ The mechanisms initiating TBI as a direct result of the shock wave generated by an explosion remain obscure, through intracranial pressure is known to be one of the major sources. Other possibilities include acceleration of the head and propagation of the blast wave to

the brain via a thoracic mechanism.⁶ Although dynamic compression, tension, and shear stress have all been proposed to explain primary TBI stemmed from direct passage of the blast wave through the cranium, the precise mechanism of how this damage arises is not fully understood.^{7,8}

The amount of pressure transmitted through the skull as a result of overpressure loading has been studied in animals and human surrogates.^{9–11} These studies have shown that the transmitted component of pressure into the brain could vary between subjects, which can be attributed to differences in experimental setup and variations in the properties of the skull and additional anatomical features. Even so, the results of these studies have demonstrated that the pressure profile varies significantly as a function of the location within the brain,^{9,11} and include both compressive (positive) and tensile (negative) pressure responses.

Numerous studies have also shown that the application of shock waves enhances the permeability of cell membranes^{8,12–15} as a result of direct mechanical poration of the neuronal cell membranes.^{16–20} Membrane disruption has the potential for either enduring membrane perturbation progressing to cell death or neuronal membrane resealing compatible with recovery.²¹ A potential consequence of transient disruption of cell membranes after blast exposure is the transport of molecules and ions including Ca^{2+} which may linger in the intercellular environment and lead to pathological irreversible changes. It is generally understood that the pores in cellular membranes, which are created during mechanical insult, serve as a major route for massive Ca^{2+} influx into brain cells after head injury. This Ca^{2+} influx triggers a cascade of events leading to cell damage and eventual cell death.²²

While it is well known that exposure of biological cells to shock waves causes damage to the cell membrane, it is still unclear by which mechanisms damage is caused and how it depends on physical parameters such as shock-wave velocity, shock-pulse duration, or shock-pulse shape. It has been suggested that shear stress generated at the shock front propagating in a heterogeneous medium can cause damage to nitrocellulose membranes.^{23,24} In general, shock waves propagate without significant energy dissipation in a homogeneous medium or media with similar acoustic impedance (i.e., water and soft tissue).⁸ However, the shock strength varies on a much smaller scale due to cellular acoustic heterogeneity, where the consequent shear – “nano-shearing” can be much larger.⁸ Ravin *et al.*⁷ found that even when the applied pressure reached 15 atm, there was no damage or excitation in human brain cells, unless shear forces are present at the cell surface, peaking between 0.3 and 0.7 Pa. Additionally, tensile stress may cause membrane damage during the shock wave propagation, since living tissue and brittle materials fail more easily under tension than under compression.²⁵ Cavitation may also occur when the frontal blast wave encounters the head and a shock wave that consists of a negative pressure portion is transmitted through the skull, cerebrospinal fluid, and tissues.

Experimentally, it is very difficult to observe the dynamics of membrane rupture due to the small time and length scales associated with the event. For instance, although the pressure front of a shock wave travels at supersonic speeds (the speed of sound in water is 1497 m/s), the shock wave generally interacts with a cell membrane, which is only several nanometers thick, during a time scale on the order of picoseconds. As a consequence, it may prove particularly helpful to elucidate the microscopic structural details and dynamics with computer simulations. Recently, there have been several computational studies on structural changes of lipid bilayers induced by shock waves,^{13,26–29} high-speed stretching,³⁰ and ultrasound radiation.³¹ Santo and Berkowitz²⁹ observed that a shock wave passing through a lipid bilayer in water induced nanobubble collapse, where they discerned transient damage to the bilayer and pore creation. After the shock wave passed the bilayer, these pores resealed and the original bilayer was recovered. Even if this poration is transient, a large amount of water was transported across the pore. Koshiyama and Wada³⁰ found that a bilayer deforms anisotropically during high-speed stretching, where they observed the formation of a water filled pore structure penetrating the bilayer develop into a large pore above a critical areal strain, resulting in rupture. In addition for high stretching speed, they observed that small pores (multipore) can temporarily form.

In this paper, shock simulations were performed on a simplified generic model of a cellular membrane using dissipative particle dynamics (DPD). In this paper, we will first describe the DPD method and our model system, where we will also discuss techniques to map DPD units to physical units for direct comparison of our results with available experimental data. We will then present calculated pressure profiles, in addition to analysis of the liposome’s structure and movement after subjection to shockwaves with low and high over pressure peaks. Structural changes of the hydrophobic layer of

the liposome as a result of impact with the shock wave were also studied to determine damage of the cellular membrane. Through this work, we determined the damage threshold in the compressive and tensile pressure for a cellular membrane. Structural changes as a result of the shock wave such as poration in the lipid layer of the liposome were also monitored. Although, the accuracy of our results is subject to the limitations of coarse-grained modeling, our results are in qualitative agreement with experiments, which also detected the existence of transient cavitation of lipid membranes.^{14,21} Future all-atom simulations will provide information for refinement of our model, leading to a better understanding of subcellular mechanisms of TBI.

II. MODEL AND METHODS

Cell membranes are mainly composed of phospholipids, each made of a hydrophilic segment (“head”) covalently bonded to a hydrophobic segment (“tail”). The phospholipids form a bilayer stabilized by hydrophobic and hydrophilic interactions. However, simulation of a realistic cell membrane is a challenging task due to the structural complexity of cell membranes. Real brain cell membranes are inhomogeneous structures that include multiple lipids, cholesterol, and numerous proteins. The goal of this research is not to simulate cell membranes in full detail, but to utilize a simplified model of the major constituent of a cell membrane, the phospholipid bilayer to study the mechanism of shock-wave-induced damage. Vesicles or liposomes are composed of phospholipids that encapsulate a core region of water inside a hydrophobic membrane. Some advantages of modeling vesicles over planar membranes, is the absence of a periodicity effect in the former, where curvature can be used as an additional parameter. Also there is closer correspondence between this spherical representation and experimental studies on vesicular systems.³² Using a coarse-grained representation also makes it feasible to simulate larger, spherical membrane systems for longer time than those accessible through an atomistic depiction. This spherical representation is necessary to reproduce qualitatively real damage processes, including membrane defects and curvature, where a less-than ideal flat surface likely contributes to membrane rupture. The longer simulation time obtainable by these models also makes it possible to study the time evolution of the shocked membranes, where the shock front can travel for a longer period of time.²⁸

The DPD approach, which is a mesoscale technique for complex fluids, correctly captures hydrodynamic behavior. A DPD system is composed of coarse-grained soft particles, each representing a cluster of molecules rather than individual atoms, moving continuously in space and discretely in time according to Newton’s equations of motion. In DPD, particles interact with each other via a pair-wise, two-body, short-ranged force, \mathbf{F} , that is written as the sum of a conservative force, \mathbf{F}^C , dissipative force, \mathbf{F}^D , and random force, \mathbf{F}^R ,

$$\mathbf{F}_i = \sum_{j \neq i} \mathbf{F}_{ij}^C + \sum_{j \neq i} \mathbf{F}_{ij}^D + \sum_{j \neq i} \mathbf{F}_{ij}^R. \quad (1)$$

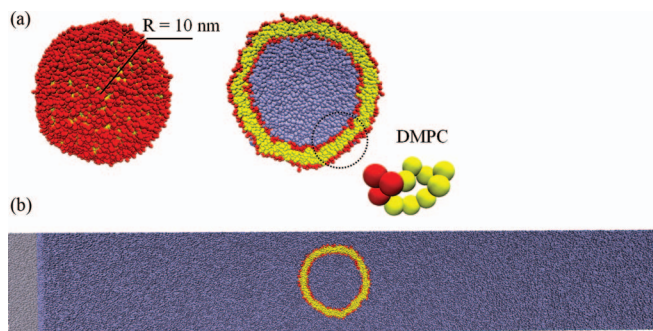


FIG. 1. (a) A representative snapshot of the (left) liposome surface and (right) cross-sectional area of the lipid vesicle: the liposome is composed of 5551 lipids. H, T, and W particles are colored red, yellow, and blue, respectively. The liposome has a radius of 10 nm (14.5 r_c in DPD units). (b) A representative cross-sectional area of the simulation box after initial compression.

\mathbf{F}^C includes a soft repulsion force which acts between two particles in addition to a harmonic force between adjacent particles in a polymer chain. \mathbf{F}^C forces are derived from interaction potentials described in Eq. (2). The remaining two forces, \mathbf{F}^D and \mathbf{F}^R , provide the DPD thermostat, which is used to maintain an average temperature of $T = 1.0$ during the course of the simulation. The dissipative force (\mathbf{F}^D) modifies the kinetic energy of the particles and is balanced by the random force (\mathbf{F}^R) according to the fluctuation-dissipation theorem. A detailed description of the DPD thermostat can be found elsewhere.^{33–36} Standard values of $m = k_B T = 1$ and overall particle density $\rho_{DPD} = 3 r_c^3$ were chosen, where the following DPD-reduced units are used: length in r_c , energy in $k_B T/r_c^2$, mass in particle mass m , and time in $\tau = r_c \sqrt{m/k_B T}$. The time step was set to $\Delta t_{DPD} = 0.01 \tau$ in DPD units, where the soft interaction forces used in our simulations allow for a much longer time step than when hard repulsion forces such as Lennard–Jones forces are utilized. Although results from DPD are sensitive to the time step,³⁷ the time step used in this study is lower than the conventional values of 0.04–0.06 τ .^{36,38} Since DPD is used to model isothermal simulations, this method may not be appropriate for capturing adiabatic processes characterized with high temperature gradients that can occur during shock wave propagation.²⁸ Because of this we will restrict our study to shock waves with low impulses (less than 10 Pa · s) that cause negligible heating of the simulation system.

The coarse-grained model that we used is based on the work of Grafmüller *et al.*³⁹ The systems considered here are constructed from three bead species: lipid head (H), lipid tail (T), and water beads (W). The model lipids have a headgroup consisting of three H beads and two hydrophobic tails, each consisting of four T beads (Figure 1(a)), which corresponds to a coarse-grained model of dimyristoyl-phosphatidylcholine (DMPC) with a $H_3(C_4)_2$ architecture. Each coarse-grained chain-bead T represents 3.5 CH_2 groups, where the level of coarse-graining, $N_m = 3.5$.

The pair interaction between topologically nonconnected particles is described by a weakly repulsive potential

$$U_{DPD}(r) = \frac{a_{DPD}}{2} \left(1 - \frac{r}{r_c} \right)^2, \quad (2)$$

TABLE I. The interaction parameters a_{ijDPD} between pairs of beads. i and j belong to head (H), tail (T), or water (W) beads, respectively.

Bead type	H	T	W
H	30	35	30
T	35	10	75
W	30	75	25

where a_{DPD} is the maximum repulsion and $r_c = 1$ is the cutoff radius. a_{DPD} differ for different bead species and their values are taken from Ref. 39. The interaction parameters are given in Table I and in general, the simulation parameters are chosen to match the mesoscopic behavior of the system.

Topologically connected beads in lipids interact according to the harmonic potential, U_{harm}

$$U_{harm}(r) = \frac{k}{2} (r - r_0)^2, \quad (3)$$

where k is the harmonic constant and r_0 is the equilibrium bond distance; the values of $k = 225 k_B T/r_c^2$ and $r_0 = 0.85 r_c$ are used. In addition, the hydrocarbon chains (tails) are stiffened by a bending potential which is enforced between two consecutive bonds

$$U_{bend}(r) = k_\theta (1 - \cos \theta), \quad (4)$$

where the potential parameters are $k_\theta = 2 k_B T$ and $\theta = 180^\circ$.

To obtain the pre-shock structure, the vesicle structure was preassembled from 5551 lipids, where the head groups were placed randomly in the inner and outer parts of the spherical membrane. Water particles were then placed randomly into the remainder of the simulation box. The hydrophobic tails of the vesicles and water particles were then equilibrated while the head beads were frozen (immobile) prior to subsequent short equilibration of the fully mobile system. The simulation box contains approximately 2 500 000 particles. This procedure produces a liposome with a radius of 10 nm (14.5 r_c in DPD units), while cells of complex organisms is on the order of micrometers. This discrepancy in size is due to restrictions in the DPD method which are constrained to length scales of $O(100 \text{ nm})$, which must account for both the water and liposome in our simulation. Even so, using a coarse-grained model such as DPD allows for a more physical description of a liposome than all atom molecular dynamics simulations which can only simulate tiny membrane patches composed of hundreds of lipid molecules.⁴⁰ A smaller representation of the liposome may lead to higher curvature and lower stability, though it is expected that trends obtained from our system will be consistent with those that would be obtained using a larger liposome.

Shock waves were initiated with a momentum reflecting mirror, which is a standard method for generating shock waves in computer simulation studies of lipid bilayers.^{13,28,29} The fast shock waves generated from this method are numerically stable and have a well-defined shock-wave front. In this method, the shock wave is created through an infinite-mass piston that moves in the positive z direction. All particles coming into contact with the piston surface are reflected, and the velocity relative to the moving wall is flipped in z .²⁸

This procedure is comparable to standard shock wave experiments where a stationary target is hit by a fast-moving impactor. Upon impact with the piston, the target material is compressed and the resulting steep density gradient initiates a shock wave. After a short initial time, the piston was stopped while the initiated shock wave continues along the z direction (Figure 1(b)).

The speed of the piston, v_p , and the final piston position were varied to produce different shock wave profiles, where the pressure was measured as function of time and z distance. The location of the liposome in the simulation box was sufficient to avoid direct impact with the piston during the shock simulation. In the first part of our study, the piston was stopped after $t = 15 \tau$, and the velocities of the piston were varied to 5, 10, 15 r_c/τ to produce shock waves with different pressure profiles. The resulting shock waves have Mach number of 1.49, 1.66, 1.76, respectively. In the second part of our study, the piston was allowed to move longer, $t = 50 \tau$, with v_p equal to 5 and 10 r_c/τ to produce higher pressure impulses. The Mach numbers of these waves are equal to 1.87 and 2.45. To calculate the Mach number, which is the ratio of the speed of the shock wave in a fluid and the local speed of sound, we took into account the speed of sound of the DPD fluid. Theoretical calculation through equation of state of a DPD fluid gives $c_{DPD} = 3.818$ DPD units, while direct estimation from simulation gives $c_{DPD} = 4.298$ in DPD units.⁴¹ For our calculations of the Mach number, we take the average value of $c_{DPD} = 4.0$.

To capture the time evolution of the shocked vesicle, the length of the simulation box in the direction of the shock impulse, L_z , must be sufficiently large to allow the shock front to travel for a long period of time. This study considers a relatively large simulation box: $50.72 \times 50.72 \times 326 r_c^3$ (corresponds to $35 \times 35 \times 225 \text{ nm}^3$), where the liposome is $29.0 r_c$ (corresponds to 20 nm) in diameter. We will discuss conversion of these DPD units into physical units in Sec. III. Non-periodic boundary conditions are utilized in all three directions in the simulation. Shrink-wrapped boundary conditions were utilized for the face that has the piston, where the position of the face is set so that it always encompasses the atoms no matter how far they move. The opposing face and the boundaries in the x and y dimensions are fixed. The simulation system was also bound with reflective walls which prevent particles from moving through the boundaries. If an atom moves outside of the wall by a distance Δx , then it is put back inside the boundary by the same distance, and the sign of the corresponding constituent of its velocity is flipped. All simulations were executed using LAMMPS software from Sandia National Laboratories.^{42,43}

III. DPD TO PHYSICAL UNITS

To compare our simulation results with experimental data, it is necessary to relate DPD units of energy, length, and time scale to physical units. The basic length scale, i.e., a physical size of interaction radius, $r_c = 0.69 \text{ nm}$, is computed to match experimental values of the area per lipid molecule. The area per molecule in the simulations is $A_{DPD} = 1.25 r_c^2$, whereas the experimentally measured value is

$A_{phys} = 0.596 \text{ nm}^2$.^{39,44} Therefore, the length scale for our simulation is $r_c = \sqrt{A_{phys}/A_{DPD}} = 0.69 \text{ nm}$.

Although the link between physical and simulation length scales is straightforward, the relationship between the experimental and computational time scales cannot be obtained directly. This is partially due to the faster dynamics observed by the coarse-grained system. The dynamics are accelerated due to the coarse-grained interaction potentials which are much smoother, therefore lowering energy barriers.⁴⁵ Thus, there is a need to compensate for this difference in dynamics by adjusting the time scale. There are several concepts, which try to map dynamics of coarse grained system with experiment, however, open questions remain.⁴⁵ One way to estimate the time scale in physical units, is to match the self-diffusion constant of a DPD particle with those obtained from a physical system,³⁶

$$\tau = \frac{N_m D_{sim} r_c^2}{D_{phys}}. \quad (5)$$

Here, we used dimyristoylphosphatidylcholine (DMPC) lipid ($D_{phys} = 5 \mu\text{m}^2/\text{s}$) as the physical system, where the in-plane diffusion coefficients for a DPD particle is $D_{sim} = 0.016 r_c^2/\tau$.³⁹ From Eq. (5), we found that the time scale $\tau = 5.3 \text{ ns}$.

In this paper, we will map differences in pressure, $\Delta P = P - P_0$ in $k_B T/r_c^3$, where P_0 is the pressure at equilibrium. Values of pressure obtained from DPD are unrealistically high even under standard conditions, for reasons we will discuss in the next paragraph. Even so, ΔP could be used to discern trends in our system, where we can use the standard conversion factor⁴⁶ $k_B T/r_c^3$, which is equal to 13 MPa for our simulation.

Even though we discuss methods to convert DPD units into physical units there is not a standardized procedure, and further research and development is still needed to fully interpret their relationship with the physical world.⁴⁷ Unfortunately, when a particular thermodynamic property of DPD is mapped to a physical system, the other properties are not guaranteed to have the correct values, due to the quadratic density dependence of the DPD equation of state. For example, it is impossible to simultaneously map the isothermal compressibility and the pressure. Typically, the DPD parameters are usually set to give the correct compressibility to obtain a lipid bilayer whose structure and dynamic properties are in good agreement with real lipid bilayers rather than the pressure. This leads to an unrealistically high pressure under standard conditions.⁴⁸ Even so, results will be presented in physical units using the conversion factors discussed in this section, so that they can be compared to available experimental data.

IV. RESULTS AND DISCUSSION

A. Pressure profile and liposome structure and movement during shock waves with low overpressure peaks

To determine the speed of the shock wave, the location of the shock wave front in z direction was identified as a function

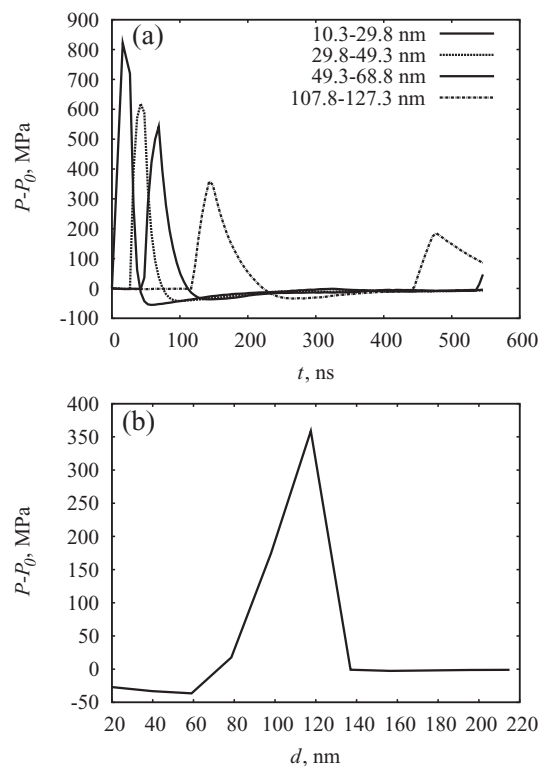


FIG. 2. (a) The supersonic shock wave at the various distances from its launch. The liposome is located at 117.4 nm. The Mach number is 1.49. (b) The pressure profile at $t = 150$ ns at the liposome location.

of simulation time. The position of the liposome was monitored during the simulation and pressure profiles were computed. This is achieved by dividing the simulation box into 11 bins, where each bin contains $\sim 250\,000$ particles. Smaller bins produce qualitatively similar results, but are more prone to statistical errors due to inadequate sampling. The initial speed of the shock wave propagation was calculated from the slope of the peak pressure versus time curve which exhibit a near-linear relationship (data not shown).

Figure 2(a) shows pressure (P) profiles obtained during the simulation at various distances, d , from the initiation of the shock wave. As expected, the peak overpressure decreases with distance from the wave initiation and causes almost instantaneous overpressure, followed by a longer interval of negative pressure. The second overpressure peak (Figure 2(a)) corresponds to the reflection and back propagation of the shock wave off of the edge of the simulation cell.

The pressure curves shown in Figure 2(a) correspond to shock waves with a Mach number, $M = 1.49$, where the Mach number is a dimensionless quantity representing the ratio of the speed of the shock wave in a fluid and the local speed of sound. The curve labeled 107.8–127.3 nm represents the change in pressure at the location of the liposome, which was placed at 117.4 nm from the center of the wave initiation, and did not move significantly. The second peak in pressure profile represents the second positive phase due to reflection from the simulation box wall. The pressure profiles that corresponds to the same system at the time of the peak overpressure ($t = 150$ ns) at the vesicle location is shown in Figure 2(b).

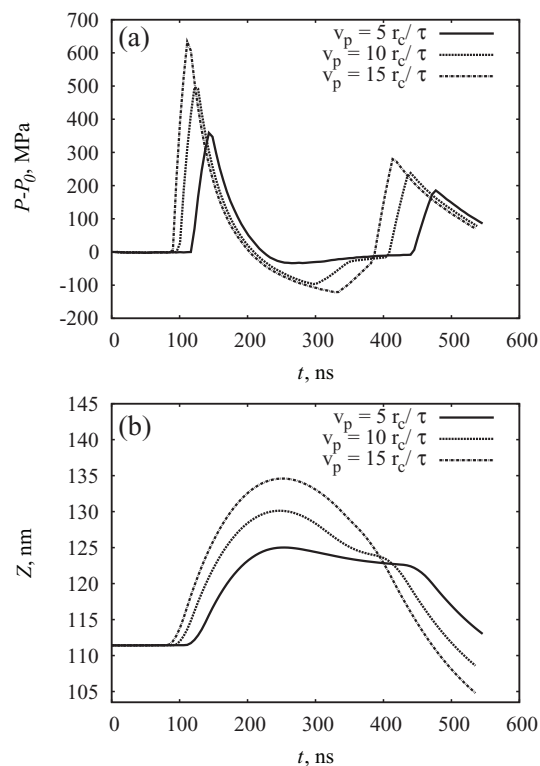


FIG. 3. (a) The shock wave at the location of the liposome for the various piston speeds v_p ; (b) movement of the center of mass of the liposome in z direction.

To produce different pressure profiles for mild shock, the piston speed v_p was varied while keeping the compression of the box constant. We considered values of v_p equal to $5 r_c/\tau$, $10 r_c/\tau$, and $15 r_c/\tau$, which produced blast waves with Mach numbers of 1.49, 1.66, 1.76, respectively. This produced shock profiles with overpressure peaks equal to 359, 495, and 633 MPa, respectively (Figure 3(a)), which were measured at the location of the liposome (approximately 117.6 nm). The piston was stopped at a distance of 107.25 nm from the liposome.

The curves shown in Figure 3(a) exhibit characteristics of extracorporeal shock waves, which are characterized by a rapid increase to a relatively high pressure (>100 MPa) in the span of a few nanoseconds, followed by an exponential descent. For these shock waves, the duration of the positive phase is on the order of 100 ns, and is followed by a comparatively small tensile wave component below ambient pressure. This negative phase can experience negative pressures up to 15 MPa, where the duration is long compared to the positive phase (around 2000 ns).^{49,50} In our simulation, the duration of the negative phase is shorter because of limitations in the simulation box size, which leads to a reflective wave earlier than the shock wave duration. The shock wave characteristics obtained in our simulations are different from blast shock waves, which are described by a lower ($O(\text{kPa})$) value of the peak pressure, where positive overpressures ΔP higher than 400 kPa are considered potentially lethal.⁵¹ Blast shock waves also exhibit a much longer positive phase duration ($O(\text{ms})$). Although, different shock waves (e.g., blast and extracorporeal) produce different pressure profiles, its impulse defined

as the pressure integrated over time is a dominant factor in changing the permeability of living cells rather than the peak pressure.¹² The impulse is computed from

$$I = \int_0^{t_+} [P(t) - P_0] dt, \quad (6)$$

where $P(t) - P_0$ is the shock wave positive overpressure and t_+ is the positive phase duration. Our simulation produced shock waves with I equal to 1.31 Pa·s, 1.93 Pa·s, and 2.49 Pa·s, respectively. The overall pressure impulse including the reflective positive phase, $I_{tot} = I_1 + I_2$ is found to be 1.87 Pa·s, 2.79 Pa·s, and 3.59 Pa·s.

When the shock wave impacts the liposome, its location slightly changes in the simulation box, where it initially moves in the positive z direction. Then, the liposome flows in the negative z direction as the reflective wave makes contact (the second positive phase). The overall movement of liposome in the lateral direction to the shock wave is found to be negligible (less than 1%). With increasing v_p , the reflective wave hits the liposome before the pressure reaches ambient value. These results show that the primary shock wave is followed by the translational motion of lipid vesicle due to inertial forces. This translational motion of the lipid vesicle is similar to a behavior of cells under shock *in vitro*, where the cells move with the surrounding liquid in the direction of the shock wave. Cells subjected to shock *in vivo* would require lower pressures or less shocks than cells *in vitro* to sustain damage and death. *In vivo*, the neighboring cells, the extracellular matrix, and basement membranes fix cells, such that when they are subjected to shock they demonstrate nonlinear, anisotropic, inhomogeneous behavior on the macroscale.¹² In the context of TBI, this linear acceleration could lead to diffuse axonal injury.⁵²

To characterize a change of the liposome size and the deviation from an equilibrium vesicle shape, the diagonal principal moments of the gyration tensor λ_{xx}^2 , λ_{yy}^2 , and λ_{zz}^2 were computed using

$$\lambda_{dd}^2 = \frac{1}{N} \sum_{i=0}^N (r_{id} - r_{com}) (r_{id} - r_{com}), \quad (7)$$

where r_{com} is the coordinates of the liposome center of mass, r_{id} is the d coordinate of bead i of the liposome, and N is number of beads in the liposome. The radius of gyration, R_g , which defines the size of the lipid vesicle is given by the sum of the principal moments,

$$R_g = \sqrt{\lambda_{xx}^2 + \lambda_{yy}^2 + \lambda_{zz}^2} \quad (8)$$

and deviation from a spherical shape for the liposome is given by the asphericity, b ,

$$b = \lambda_{zz}^2 - 0.5 (\lambda_{xx}^2 + \lambda_{yy}^2). \quad (9)$$

Figure 4 shows the change in R_g and b with time, where we observed that changes in size of liposome are accompanied by changes in its shape. Initially, the liposome is compressed during the positive pressure phase, where R_g is changed by 10.3%, 11.6%, and 12.7%, respectively. After

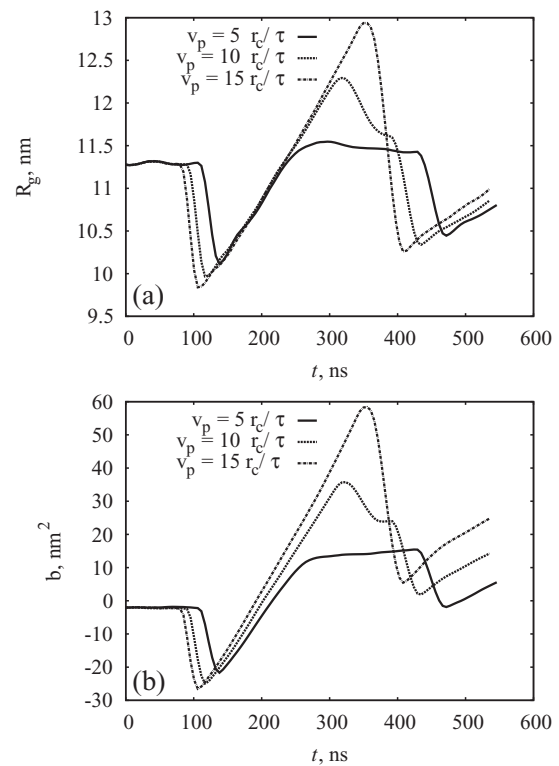


FIG. 4. Change of liposome size and shape vs time. (a) Radius of gyration of the liposome, R_g and (b) asphericity, b .

compression the liposome undergoes extension during the negative pressure phase, where R_g is increased by 2.0%, 9.0%, and 14.7% compared with its initial size (Figure 4(a)). During the reflective wave, the process repeats with lower values for both compression and extension. Notably, the extent of liposome compression does not strongly depend on the pressure pulse compared with an extent of liposome extension (Figure 4(b)). This finding suggests that liposome extension is very sensitive to the change in the negative pressure phase, which can consequently lead to more structural damage of the cell membranes. This is consistent with the general properties of living tissues, which fail more easily under tension than under compression.²⁵

B. Pressure profile and liposome structure and movement during shock waves with high overpressure peaks

To produce higher overpressure, two simulations were performed with piston speeds v_p equal to $5 r_c / \tau$ and $10 r_c / \tau$, respectively. In these simulations, the piston was allowed to move longer and the piston was stopped at the distance of 83.1 nm from the liposome. Therefore, the positive pressure phase values are greater than those reported in Sec. IV A though the negative pressure values are not significantly smaller (cf. Figures 3(a) and 5(a)). The Mach numbers of these waves are equal to 1.87 and 2.45 for v_p values $5 r_c / \tau$ and $10 r_c / \tau$, respectively. Since the shock waves move faster in these simulations, the reflection wave reaches the liposome earlier than in the previous simulations, though the durations of the

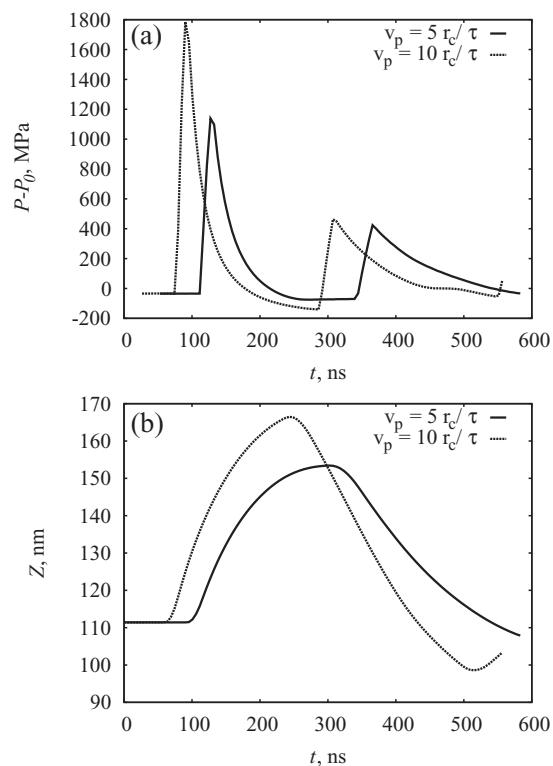


FIG. 5. (a) The shock wave at the location of the liposome for the various piston speeds v_p . (b) Movement of the center of mass of the liposome in z direction.

positive and negative phases are similar (cf. Figures 3(a) and 5(a)). In the case of the fastest shock wave with Mach number of 2.45, one can see the emergence of a third pressure peak that corresponds to the second reflective wave. In addition, the liposome travels a greater distance in the positive z direction than the shock waves discussed in Sec. IV A which have a lower overpressure peak (cf. Figures 3(b) and 5(b)). The positive impulse of these shock waves is found to be $3.33 \text{ Pa} \cdot \text{s}$ and $5.57 \text{ Pa} \cdot \text{s}$ for v_p values $5 r_c / \tau$ and $10 r_c / \tau$, respectively, for the first overpressure peak. I_{tot} for these waves are $4.91 \text{ Pa} \cdot \text{s}$ and $7.09 \text{ Pa} \cdot \text{s}$ for v_p values $5 r_c / \tau$ and $10 r_c / \tau$, respectively.

The size and shape of the liposome changes similar to those associated with the slower moving waves during initial impact of the shock wave (Sec. IV A), but the reflective portion of the shock waves has a stronger impact on the liposome size (cf. Figures 4 and 6). Interestingly, the liposome undergoes less movement in the z direction for $v_p = 10 r_c / \tau$ than $v_p = 5 r_c / \tau$ (Figure 6(b)). This is caused by the reflective wave that reaches the liposome before the vesicle was fully stretched.

C. Structural changes of hydrophobic layer of the liposome

We observe damage in the lipid layer of the vesicle as a result of impact with the shock wave (Figure 7(a)). Since the hydrophobic layer of the liposome is more fluidic than the polar layer, the hydrophobic layer should be damaged at a lower pressure, which we observe in our simulation. This damage

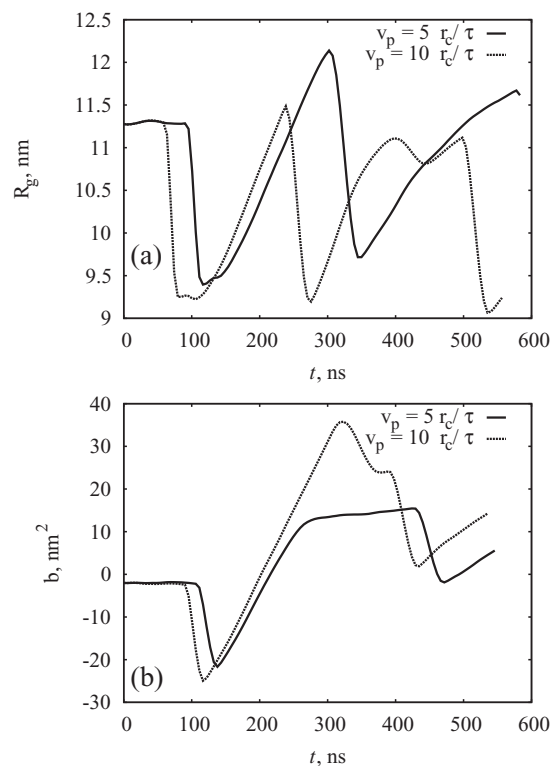


FIG. 6. Change of liposome size and shape vs time. (a) Radius of gyration of the liposome, R_g and (b) asphericity, b .

will alter the membrane permeability, which we characterize by assessing the hydrophobic layer structure.

To do this, we use the concept of a “negative” or inverted image. Namely, we consider any space that is not populated by hydrophobic beads as being “occupied” by dummy particle, where the size of this particle is equal to the size of the empty space. This is achieved by dividing the spherical hydrophobic layer into bins, with a grid spacing of $0.69 \times 0.69 \text{ nm}$, which is the minimal space resolution available for this model (see Sec. II). Space adjacent to the outer and inner part of the hydrophobic layer is also divided in the same manner, though the thickness was chosen to be twice the bin size to reduce computational burden.

This calculation was achieved through software developed in-house⁵³ which identified the size and number of all connected voids during the simulation. For each snapshot of the trajectory, “empty” bins that were not populated by any hydrophobic beads were calculated. If the empty bins are

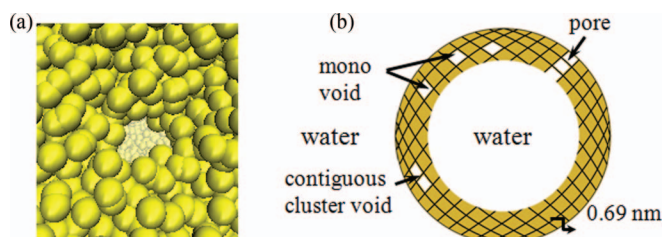


FIG. 7. (a) The snapshot of a pore in the hydrophobic layer of the lipid vesicle. W and H beads removed for clarity. (b) Schematic of possible damage of the hydrophobic layer.

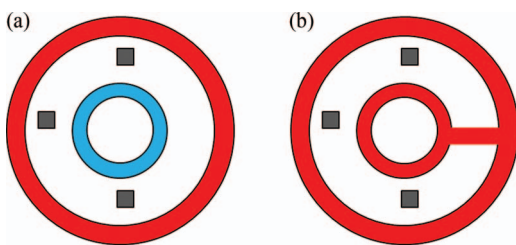


FIG. 8. Schematic representation of our method. (a) Two large clusters are present; they are composed from adjacent outer and inner layers and colored in red and blue, respectively. Small cluster voids are colored in grey. (b) The liposome has a pore and one large cluster colored in red is present along with some number of small clusters.

solitary, i.e., they do not neighbor any other empty bins, we identify them as mono voids. Second, we identified clusters made of the empty bins, where contiguous cluster voids arise from several connected voids.

At the start of the simulation (before any impact of the shock wave), two big clusters of dummy particles are present, which correspond to inner and outer adjacent layers to the hydrophobic part of the liposome (see Figure 8). Even before impact, some number of mono voids may be present. Upon impact, the number of mono voids could change and small contiguous cluster voids can form. The small cluster voids are composed of 2 empty bins, where the large clusters can vary in size, but are always larger than 3000 bins. There are no clusters composed of empty bins between 2 and 3000. When a pore forms, contiguous void traverses the hydrophobic layer, and the outer and inner adjacent layers become connected such that one very big cluster of dummy particles is formed (see Figure 8(b)). Thus, a pore in the vesicle links water inside of liposome with water from the outside through a series of connected empty bins (Figure 7(b)).

Figure 9 shows the change in the number of voids in the hydrophobic layer, N_v , with time, t , during propagation of the

shock wave for our systems with low overpressure peaks. For the lowest overpressure peak, $P_{max} = 358$ MPa, there are no significant change in the structure (Figure 9(a)), where only the formation of mono voids was observed. While N_v at compression is slightly reduced compared with N_v prior the shock, N_v at extension $P_{min} \approx -34$ MPa is slightly higher and could suggest the onset of membrane disruption due to cavitation. This agrees with Lin *et al.* who determined that for very short pulse shock waves that the intrinsic cavitation threshold is 26–35 MPa.⁵⁴ When the pressure profile has a higher peak, $P_{max} = 495$ MPa, the number of mono voids is significantly increased under extension, which corresponds to the negative portion of the pressure profile, where a few contiguous cluster voids also appear. The maximum number of mono voids occurs at the pressure minimum, where the liposome is the most extended. At both of the positive pressure peaks, $N_v = 0$, which corresponds to significant compression of the vesicle (Figure 9(b)). For the pressure profile with $P_{max} = 633$ MPa, we observed a similar outcome, but we detected the formation of a pore under the extension, where $P_{min} = -121$ MPa. This pore was transient and closed as the reflective compressive pressure reached the liposome. Thus, our results suggest that the lipid membranes are more sensitive to tensile than to compressive deformation, where our results indicate that the pressure threshold for mechanical poration of a lipid membrane is $P_{ext} \approx 121$ MPa under tensile deformation.

Interestingly, a higher overpressure peak, $P_{max} = 1140$ MPa (Figure 10(a)), that corresponds to $I = 3.33$ Pa · s does not produce significant damage to the lipid membrane, but impact with the second reflective positive peak of pressure, $P_{ref} = 423.7$ MPa results in pore formation, which lingers even after the reflective wave passes through the liposome and the pressure values are significantly reduced (Figure 10(a)). In this case, the overall pressure impulse is 4.91 Pa · s. The negative pressure values were smaller than P_{ext} , thus no pores were formed at the extension phase of the shock wave. Our

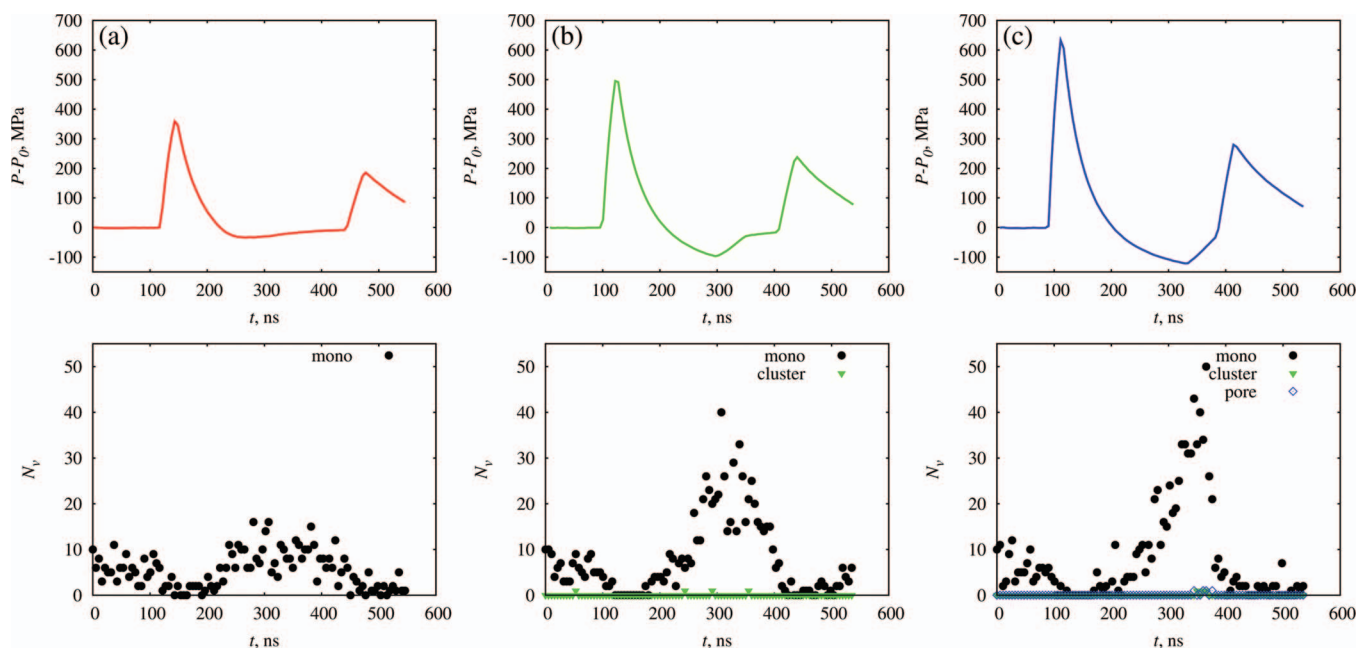


FIG. 9. (a)–(c) Number of voids in the hydrophobic layer as function of pressure profile.

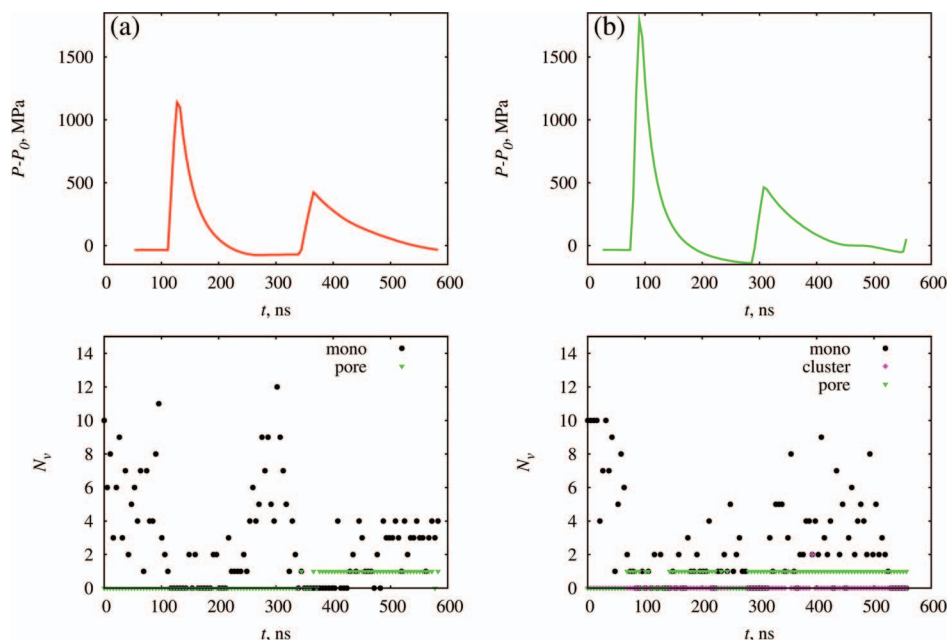


FIG. 10. (a) and (b) Number of voids in the hydrophobic layer as function of pressure profile.

results also show that damage to the cellular membrane occurs for lower pressures under repetitive exposure, which is in agreement with experimental observation.¹⁴ We observed creation of the pore in the lipid vesicle during the positive pressure phase for the largest peak pressure of $P_{max} = 1786$ MPa which corresponds to pressure impulse of $I = 5.57$ Pa \cdot s ($I_{tot} = 7.09$ Pa \cdot s). Also, these pores did not re-seal during the simulation. Thus, our results indicate that direct poration for lipid bilayer occurs for pressure impulse values higher than 5 Pa \cdot s. Our results are in good agreement with experiment¹² which have shown that fluorescence uptake, which is related to cell permeability, starts to change around 5 Pa \cdot s.

V. CONCLUSION

TBI is a major health issue that is hard to diagnose since it often occurs without signs of external injuries. While it is well known that exposure of biological cells to shock waves causes damage to the cell membrane, it is currently unknown by which mechanisms damage is caused, and how it depends on physical parameters such as shock wave velocity, shock pulse duration, or shock pulse shape. In this computational study, we used a coarse-grained model of a lipid vesicle as a generic model of a cell membrane to elucidate the general principles of the cellular damage induced by the shock wave direct passage through the cranium. Results indicate that the extent of liposome compression does not strongly depend on the pressure pulse and that liposome extension is very sensitive to changes in the negative pressure phase. In addition, the structural integrity of the vesicle is altered as pores form in the lipid membrane at pressures generated by supersonic shock waves, when the pressure impulse of the shock wave is greater than 5 Pa \cdot s. Even so, damage to the lipid membrane may arise at lower compressive pressure under repetitive exposure, if the overall pressure impulse is greater than 5 Pa \cdot s. Consequently, these changes in permeability may lead to an

influx of sodium, potassium, and calcium ions, which can lead to cell death. Direct poration also can occur during the tensile portion of the blast wave, but only for very high negative pressure values $P_{ext} \approx -120$ MPa. Although, the accuracy of our results is subject to the limitations of coarse-grained modeling, our results are in qualitative agreement with experiments, such as those that consider the existence of transient cavitation in lipid membranes.²¹ Future all-atom simulations will provide information for refinement of our model, leading to a better understanding of subcellular mechanisms of TBI.

ACKNOWLEDGMENTS

The authors would like to thank Dr. J. W. Andzelm, Dr. R. Banton, Dr. P. Franaszczuk, Dr. T. Piehler, Dr. J. Vettel, and Dr. N. Zander for useful discussion. Calculations were performed on DOD High Performance Computing site at the AFRL through the Challenge Project C5M.

The research reported in this document was performed in connection with contract/instrument W911QX-14-C-0016 with the U.S. Army Research Laboratory.

The views and conclusions contained in this document are those of the authors and should not be interpreted as presenting the official policies or position, either expressed or implied, of the U.S. Army Research Laboratory or the U.S. Government unless so designated by other authorized documents.

¹M. F. Weiner and A. M. Lipton, *The American Psychiatric Publishing Textbook of Alzheimer Disease and Other Dementias* (American Psychiatric Publishing, Virginia, 2009).

²C. C. Duncan, A. C. Summers, E. J. Perla, and K. L. Coburn, *Int. J. Psychophysiol.* **82**, 24 (2011).

³R. K. Gupta and A. Przekwas, *FNEUR* **4**, 1 (2013).

⁴I. G. Bowen, E. R. Fletcher, D. R. Richmond, F. G. Hirsch, and C. S. White, *Ann. N. Y. Acad. Sci.* **152**, 122 (1968).

⁵H. J. Thompson, J. Lifshitz, N. Marklund, M. S. Grady, D. I. Graham, D. A. Hovda, and T. K. McIntosh, *J. Neurotrauma* **22**, 42 (2005).

- ⁶A. C. Courtney and M. W. Courtney, *Med. Hypotheses* **72**, 76 (2009).
- ⁷R. Ravin, P. S. Blank, A. Steinkamp, S. M. Rappaport, N. Ravin, L. Bezrukov, H. Guerrero-Cazares, A. Quinones-Hinojosa, S. M. Bezrukov, and J. Zimmerberg, *Plos One* **7**, e39421 (2012).
- ⁸A. Nakagawa, G. T. Manley, A. D. Gean, K. Ohtani, R. Armonda, A. Tsukamoto, H. Yamamoto, K. Takayama, and T. Tominaga, *J. Neurotrauma* **28**, 1101 (2011).
- ⁹M. Chavko, W. A. Koller, W. K. Prusaczyk, and R. M. McCarron, *J. Neurosci. Meth.* **159**, 277 (2007).
- ¹⁰A. Säljö, F. Arrhen, H. Bolouri, M. Mayorga, and A. Hamberger, *J. Neurotrauma* **25**, 1397 (2008).
- ¹¹J. K. Shridharani, G. W. Wood, M. B. Panzer, B. P. Capehart, M. K. Nyein, R. A. Radovitzky, and C. R. Bass, *Front Neurol.* **3**, 1 (2012).
- ¹²T. Kodama, M. R. Hamblin, and A. G. Doukas, *Biophys. J.* **79**, 1821 (2000).
- ¹³K. Koshiyama, T. Kodama, T. Yano, and S. Fujikawa, *Biophys. J.* **91**, 2198 (2006).
- ¹⁴P. Arun, R. Abu-Taleb, M. Valiyaveetil, Y. Wang, J. B. Long, and M. P. Nambiar, *Neuroreport* **2**, 342 (2012).
- ¹⁵P. Arun, R. Abu-Taleb, S. Oguntayo, M. Tanaka, Y. Wang, M. Valiyaveetil, J. B. Long, Y. Zhang, and M. P. Nambiar, *Neurosci. Lett.* **552**, 87 (2013).
- ¹⁶E. H. Pettus, C. W. Christman, M. L. Giebel, and J. T. Povlishock, *J. Neurotrauma* **11**, 507 (1994).
- ¹⁷M. C. LaPlaca, V. M. Lee, and L. E. Thibault, *J. Neurotrauma* **14**, 355 (1997).
- ¹⁸D. M. Geddes, R. S. Cargill II, and M. C. LaPlaca, *J. Neurotrauma* **20**, 1039 (2003).
- ¹⁹G. R. Prado, J. D. Ross, S. P. DeWeerth, and M. C. LaPlaca, *J. Neural. Eng.* **2**, 148 (2005).
- ²⁰R. H. Singleton and J. T. Povlishock, *J. Neurosci.* **24**, 3543 (2004).
- ²¹O. Farkas, J. Lifshitz, and J. T. Povlishock, *J. Neurosci.* **26**, 3130 (2006).
- ²²J. T. Weber, *Front. Pharmacol.* **3**, 1 (2012).
- ²³L. Hesselink and B. Sturtevant, *J. Fluid Mech.* **196**, 513 (1988).
- ²⁴D. Howard and B. Sturtevant, *Ultrasound Med. Biol.* **23**, 1107 (1997).
- ²⁵X. Xi and P. Zhong, *J. Acoust. Soc. Am.* **109**, 1226 (2001).
- ²⁶K. Koshiyama, T. Kodama, T. Yano, and S. Fujikawa, *Biochim. Biophys.* **1778**, 1423 (2008).
- ²⁷A. Choubey, M. Vedadi, K. Nomura, R. K. Kalia, A. Nakano, and P. Vashishta, *Appl. Phys. Lett.* **98**, 023701 (2011).
- ²⁸G. C. Canzenmüller, S. Hiermaier, and M. O. Steinhauser, *Soft Matter* **7**, 4307 (2011).
- ²⁹K. P. Santo and M. L. Berkowitz, *J. Chem. Phys.* **140**, 054906 (2014).
- ³⁰K. Koshiyama and S. Wada, *J. Biomech.* **44**, 2053 (2011).
- ³¹K. Koshiyama, T. Yano, and T. Kodama, *Phys. Rev. Lett.* **105**, 018105 (2010).
- ³²S. J. Marrink, A. H. de Vries, and D. P. Tieleman, *Biochim. Biophys.* **1788**, 149 (2009).
- ³³P. J. Hoogerbrugge and J. M. V. A. Koelman, *Europhys. Lett.* **19**, 155 (1992).
- ³⁴J. M. V. A. Koelman and P. J. Hoogerbrugge, *Europhys. Lett.* **21**, 363 (1993).
- ³⁵P. Español and P. B. Warren, *Europhys. Lett.* **30**, 191 (1995).
- ³⁶R. D. Groot and K. L. Rabone, *Biophys. J.* **81**, 725 (2001).
- ³⁷J. F. Peters, *Europhys. Lett.* **66**, 311 (2004).
- ³⁸R. D. Groot and P. B. Warren, *J. Chem. Phys.* **107**, 4423 (1997).
- ³⁹A. Grafmüller, J. Shillcock, and R. Lipowsky, *Biophys. J.* **96**, 2658 (2009).
- ⁴⁰V. Ortiz, S. O. Nielsen, D. E. Discher, M. L. Klevin, R. Lipowsky, and J. Shillcock, *J. Phys. Chem. B* **109**, 17708 (2005).
- ⁴¹J. S. Soares, C. Gao, Y. Alemu, M. Slepian, and D. Bluestein, *Ann. Biomed. Eng.* **41**, 2318 (2013).
- ⁴²S. Plimpton, *J. Comput. Phys.* **117**, 1 (1995).
- ⁴³Sandia Laboratories Home Page, LAMMPS Molecular Dynamics Simulator, see <http://lammps.sandia.gov> (accessed on 10/30/2013).
- ⁴⁴J. F. Nagle and S. Tristram-Nagle, *Biochim. Biophys. Acta* **1469**, 159 (2000).
- ⁴⁵D. Fritz, K. Koschke, V. A. Harmandaris, N. F. A. van der Vegt, and K. Kremer, *Phys. Chem. Chem. Phys.* **13**, 10412–10420 (2011).
- ⁴⁶A. Ghoufi, J. Emile, and P. Malfreyt, *Eur. Phys. J. E* **36**, 10 (2013).
- ⁴⁷J. K. Brennan and M. Lisal, *Mol. Simul.* **35**, 766 (2009).
- ⁴⁸S. Y. Trofimov, “Thermodynamic consistency in dissipative particle dynamics,” (Department of Applied Physics, Technische Universiteit Eindhoven, Eindhoven, 2003).
- ⁴⁹O. Wess, *ISMST* **1**, 5 (2006).
- ⁵⁰D. M. Wilbert, *BJU Int.* **90**, 507 (2002).
- ⁵¹S. Glasstone and P. J. Dolan, *The Effects of Nuclear Weapons* (US Department of Defense, Washington, DC, 1977).
- ⁵²D. H. Smith and D. F. Meaney, *Neuroscientist* **6**, 483 (2000).
- ⁵³Y. R. Sliozberg, K. E. Strawhecker, J. W. Andzelm, and J. L. Lenhart, *Soft Matter* **7**, 7539 (2011).
- ⁵⁴K.-W. Lin, Y. Kim, A. D. Maxwell, T.-Y. Wang, T. L. Hall, Z. Xu, J. B. Fowlkes, and C. Cain, *IEEE Trans. Ultrason. Ferroelectr. Freq. Control* **61**, 251 (2014).